
Quantifying error in estimates of human brain fiber directions using Earth Mover's Distance

Charles Y. Zheng
 Department of Statistics
 Stanford University
 Stanford, CA 94305
 snarles@stanford.edu

Franco Pestilli
 Department of Psychological and Brain Sciences
 Indiana University
 Bloomington, IN 47405
 franpest@indiana.edu

Ariel Rokem
 Department of Psychology
 Stanford University
 Stanford, CA 94305
 arokem@stanford.edu

Abstract

Diffusion-weighted MR imaging (DWI) is the only method we currently have to measure connections between different parts of the human brain *in vivo*. To elucidate the structure of these connections, algorithms for tracking bundles of axonal fibers through the subcortical white matter rely on local estimates of the *fiber orientation distribution function* (fODF) in different parts of the brain. These functions describe the relative abundance of populations of axonal fibers crossing each other in each location. Multiple models exist for estimating fODFs. The quality of the resulting estimates can be quantified by means of a suitable measure of distance on the space of fODFs. However, there are multiple distance metrics that can be applied for this purpose, including smoothed L_p distances and the Wasserstein metrics. Here, we give four reasons for the use of the Earth Mover's Distance (EMD) equipped with the arc-length, as a distance metric. First, the EMD is an extension of the intuitive angular error metric, often used in the DWI literature. Second, the EMD is equally applicable to continuous fODFs or fODFs containing mixtures of Dirac deltas. Third, the EMD does not require specifying smoothing parameters. Finally, the EMD is useful in practice, as well as in simulations. This is because the error of an estimated fODF, as quantified by the EMD of this fODF from the ground truth is correlated with the replicate error: the EMD between the fODFs calculated on two repeated measurements. Though we cannot calculate the error of the estimate directly in experimental data measured *in vivo* (in contrast to simulation in which ground truth is known), we can use the replicate error, computed using repeated measurements, as a surrogate for the error. We demonstrate the application of computing the EMD-based replicate error in MRI data, creating anatomical contrast that is not observed with an estimate of model prediction error.

1 Introduction

Diffusion-weighted magnetic resonance imaging (DWI) is a biomedical imaging technique that creates images that are sensitive to the direction and distance of water diffusion within millimeter-scale voxels in the human brain *in vivo*. Repeated in several different directions, diffusion sensitization can be used to make inferences about the microstructural properties of brain tissue in different loca-

tions, about the trajectories of organized bundles of axons, or fascicles, and about the connectivity structure of the brain. This is because water molecules freely diffuse along the length of nerve cell axons, but are restricted by cell membranes and myelin along directions orthogonal to the axon’s trajectory. This technique has therefore been used in many clinical and basic research applications [1].

To make inferences about the directions and relative fractions of different fascicles within each region of the brain, mixture models are employed. The signal within each volumetric pixel (or voxel) of approximately $2 \times 2 \times 2 \text{ mm}^3$ is deconvolved with a kernel function, f_κ , assumed to represent the signal from every individual fascicle [2]. A set of weights, w_i provides an estimate of the fiber orientation distribution function (fODF) in each voxel, a representation of the direction and volume fraction of different fascicles in each voxel. However, many algorithms are proposed to perform this deconvolution. In choosing a model and an algorithm, the main consideration is the *accuracy* of the model with respect to the ground truth. Accuracy is defined as the average *error* of the model fit to the ground truth; error can be assessed by comparing model fits with a known physical structure, such as excised neural tissue that is placed in the MRI device in a particular configuration [3]. However, direct assessment of error, and hence model accuracy, is not applicable in human brain *in vivo*. Hence, a useful proxy for accuracy is the *precision*, or equivalently, the *reliability* of the model—how much the model fit varies due to noise. Precision can be estimated by fitting the model to several replicate datasets with independent noise; computing the difference between the fitted models produces a quantity which we refer to as the *replicate error*. While precision does not guarantee accuracy, the inverse statement holds—an *imprecise* model will also be *inaccurate*.

Both *error* and *replicate error* require the specification of a distance function or divergence on the space of fODFs. In turn, we can quantify *model inaccuracy* as average error and *model imprecision* as average replicate error.¹ Previous DWI studies have used numerical simulations to assess the fits of algorithms to the fODF [2, 4, 5], and the angular error (AE), quantified as the sum of the minimal arc distances between the true directions and estimated directions, is commonly used as a measure of inaccuracy in these studies. AE has an intuitive appeal, but its application to fODFs with multiple non-zero weights is problematic, since angular error ignores the relative weights of the directions, and also fails to penalize fODFs with an incorrect number of directions. However, the fODF is naturally interpreted as a probability distribution of directions. Thus, any distance between probability distributions could be used to measure distances between fODFs. In the present study, we examine three commonly used distances or divergences: total variation (TV), Kullback-Leibler divergence (KL), and earth mover’s distance (EMD). We demonstrate that the EMD has several advantages over other measures of discrepancy between fODFs.

2 Methods and Theory

2.1 Models

We model the diffusion signal using a *sparse fascicle model* (SFM). Originating from work by [6] and further developed by Behrens et al, Dell’Acqua et al and Tournier et al [2, 7, 8], these models describe every voxel of the white matter as composed of k distinct populations of fibers, where k is an integer greater or equal to 1. The directions of the fibers are unit vectors v_1, \dots, v_k , and we do not distinguish between a vector v and its mirror image $-v$, because DWI measurements are antipodally symmetric. The weights of the fibers are real positive numbers w_1, \dots, w_k and add to 1, reflecting the fractional volume occupied by the fiber population. The signal measured in direction x_i is:

$$y_i \sim \text{Rician}(\tilde{S}_0 \sum_{j=1}^k w_j e^{-\kappa(v_j^T x_i)}, \sigma^2)$$

¹ Note that the definition of accuracy and precision resemble but subtly differ from the statistical concepts of *bias* and *variance*. Bias refers to the difference between the average model fit and the ground truth. However, in non-Euclidean spaces, there may not exist an operation for averaging multiple model fits, making the concept of bias inapplicable. Meanwhile, variance is defined as half the average *squared* distance between two model fits, in contrast to imprecision, which is the average distance between two model fits.

where \tilde{S}_0 is a scaling parameter, κ is a free parameter which is assumed constant given fixed experimental parameters (gradient field strength, pulse duration, etc.), and the Rician distribution [9] is defined by $\sqrt{(\mu + Z_1)^2 + Z_2^2} \sim \text{Rician}(\mu, \sigma^2)$ for $Z_i \stackrel{iid}{\sim} N(0, \sigma^2)$.

Under the general framework of the SFM, one arrives at more specific models by making particular assumptions about the number of fibers and their properties. One might assume the assumption of a particular lower bound for the angular separation between distinct fiber populations, a minimal threshold on the proportion of a fiber in a voxel, or an upper limit on the number of distinct fibers in a voxel. Furthermore, it is necessary to specify the parameter κ ; one can estimate κ from the data, or rely on a biophysical model. In the simulation studies, we will treat κ and σ^2 as known parameters.

The SFM can be formulated as a Bayesian model, by specifying priors on the number of fibers, the directions of the fibers, and the weights of the fibers. For reasons of computational tractability, we assume $k = 2$ fibers and that each fiber has a weight of 0.5, with a direction which is independently uniformly distributed. The posterior distribution for this model can be easily computed, by discretizing the projective plane. Supposing the data is also generated by the same priors, the Bayesian posterior allows one to obtain optimal point estimates. However, one could consider the Bayesian model as a useful approximation to the truth even when the priors are incorrect.

Inference of the SFM is simplified considerably if one is willing to model the signal as having a Gaussian distribution rather than a Rician distribution. Under the assumption of Gaussianity, the fODF \hat{f} is estimated through non-negative least squares (NNLS):

$$\hat{f} = \sum_{j=0}^p \frac{\beta_j}{\sum_i \beta_i} \delta_{u_j}$$

$$\beta = \operatorname{argmin}_{\beta > 0} \sum_{i=1}^n \left| y_i - \sum_{j=1}^p \beta_j e^{-\kappa(u_j^T x_i)} \right|^2 \quad (1)$$

where u_1, \dots, u_p are points from an arbitrarily fine sampling of the projective plane.² The NNLS method does not constrain the number of directions with positive weights. However, one can choose to use best- \hat{K} -subset regression (BKS)³ to constrain the number of directions to \hat{K} : $\beta = \operatorname{argmin}_{\beta > 0, \|\beta\|_0 = \hat{K}} \sum_{i=1}^n \left| y_i - \sum_{j=1}^p \beta_j e^{-\kappa(u_j^T x_i)} \right|^2$. Here $\|\cdot\|_0$ is the L_0 pseudonorm, which counts the number of nonzero components in the vector.

Figure 1 illustrates example fODFs estimated by the Bayesian posterior mean, NNLS and best-2-subset regression (B2S).

2.2 Distances for Probability Distributions

The total variation metric for distributions P and Q is defined as $d_{TV}(P, Q) = \sup_A |P(A) - Q(A)|$ where A is an arbitrary measurable set and is easy to compute: Given vectors p and q which are histograms for P and Q respectively, TV is approximated by $\frac{1}{2} \|p - q\|_1$, with $\|\cdot\|_1$ the L_1 vector norm. Another commonly used characterization of distance between distributions is the Kullback-Leibler divergence: $KL(P, Q) = \int \log(dP/dQ) dP$. We will use the symmetrized KL divergence, defined by $SKL(P, Q) = \frac{1}{2} KL(P, Q) + \frac{1}{2} KL(Q, P)$. Note that while TV is a distance metric, neither KL divergence nor symmetrized KL divergence are metric. Both TV and KL divergence are unsuitable to compare distributions which are mixtures of Dirac delta function. If P and Q are two distributions with disjoint support, the total variation distance $d_{TV}(P, Q)$ will be equal to 1, while

² It is common to apply regularization, such as an L_1 penalty [2], or elastic net penalty [12], to the objective function (1). However, NNLS yields useful estimates even without regularization; hence we neglect the regularized variants of NNLS in this paper.

³ Finding the best set of \hat{K} directions is an NP-hard problem in general. However, two considerations make it feasible in the application of DWI imaging. One, there are scientific reasons to assume that \hat{K} is a small number, e.g. from two five. Two, we are willing to tolerate a small angular error in the chosen directions. These two factors mean that a brute force search is possible, though still computationally expensive. This is in contrast to the general problem of best subset regression, which often requires the use of greedy search or convex approximation.

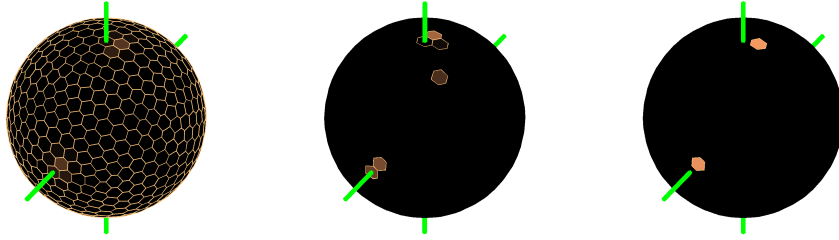


Figure 1: fODFs estimated by the Bayesian posterior mean (left), NNLS (center), and Best-2-subset regression (B2S; right) given the same data. Sticks indicate true directions entered into simulation. Light edges on polygons indicate positive probability mass. At the one end, the Bayesian posterior mean is continuous, while at the other, B2S produces a very sparse estimate, with NNLS having intermediate sparsity.

the KL divergence $KL(P, Q)$ will be infinite, regardless of how close or how far the atoms of P and Q are from each other. Therefore, rather than applying total variation or KL divergence directly, one can first apply *kernel smoothing* to the distributions, then compute the distance between the smoothed fODFs [10]. Here, we use Gaussian smoothing, parameterized by $\lambda > 0$, and we write the convolution of P with the gaussian kernel with mean zero and variance λ^{-1} by $P \star \phi_\lambda$. Hence we define the smoothed TV distance as $d_{TV, \lambda}(P, Q) = d_{TV}(P \star \phi_\lambda, Q \star \phi_\lambda)$ and the smoothed symmetrized KL divergence as $SKL_\lambda(P, Q) = SKL(P \star \phi_\lambda, Q \star \phi_\lambda)$. Figure 2 illustrates the calculation of smoothed TV distance in a one-dimensional setting.

The earth mover’s distance (EMD), or 1-Wasserstein distance, can be interpreted as the minimal amount of work needed to transform P_1 into P_2 , by optimally transporting the mass from P_1 to the mass in P_2 . The work is measured by the total distance times mass transported; a general definition can be found in [11]. Figure 2 illustrates the calculation of EMD in a one-dimensional setting. In contrast to the TV distance or the KL divergence, the EMD depends on the notion of a distance or cost between two points: in other words, it incorporates the geometry of the underlying space. The EMD between two distributions P_1 and P_2 can be computed by linear programming in the special case that P_1 and P_2 are mixtures of Dirac deltas; i.e., $P_i = \sum_{j=1}^{k^i} w_j^i \delta_{v_j^i}$. Then

$$d_{EMD}(P_1, P_2) = \min_x \sum_{i=1}^{k^1} \sum_{j=1}^{k^2} c_{ij} x_{ij} \text{ subject to } x_{ij} \geq 0, \sum_{i=1}^{k^1} x_{ij} = w_j^2, \sum_{j=1}^{k^2} x_{ij} = w_i^1 \quad (2)$$

where $c_{ij} = d(v_i^1, v_j^2)$ for a suitable distance metric d . Here x_{ij} is understood as the amount of mass moved from the point v_i^1 in P_1 to the point v_j^2 in P_2 .

The 2-Wasserstein distance (2WD) has a similar definition to EMD, replacing d_{EMD} with d_{Was2}^2 and replacing c_{ij} with c_{ij}^2 in equation (2).

Because the EMD and 2-Wasserstein distance (2WD) are equipped with a notion of geometrical distance, either can be used to quantify how two mixtures of Dirac delta functions are “close” even though none of the delta functions overlap, and in contrast to the KL and TV metrics, does not require the choice of an arbitrary smoothing parameter.

It is possible to state a number of additional properties of the aforementioned distance metrics when they are applied in Euclidean space.

First is the concept of *scale equivariance*. Given a probability distribution P , one can define *scaling* by a constant $\lambda > 0$ by defining the scaling measure λP

$$(\lambda P)(A) = P\left(\frac{1}{\lambda} A\right)$$

recalling that λA is defined as $\lambda A = \{\lambda x : x \in A\}$. Then the property of scale equivariance is defined as

$$d(P, Q) = \frac{1}{\lambda} d(\lambda P, \lambda Q)$$

for all probability distributions P, Q . It is easy to prove that EMD and 2-Wasserstein distance satisfy scale equivariance. Meanwhile, total variation satisfies *scale invariance* rather than scale equivariance, which is the property that

$$d(P, Q) = d(\lambda P, \lambda Q).$$

But smoothed total variation satisfies neither scale equivariance nor scale invariance, due to the smoothing parameter.

The second concept is that of *robustness to outliers*. Given a probability distribution P with mass concentrated in a small ball (say, the unit ball), one can consider *contamination* of the distribution with a point mass located at a distant point x . That is, consider transforming P to $(1 - \epsilon)P + \epsilon\delta_x$ for x with $\|x\|$ large. The robustness of the distance metric d is determined by the behavior of the quantity

$$d(P, (1 - \epsilon)P + \epsilon\delta_x)$$

as $\epsilon \rightarrow 0, \|x\| \rightarrow \infty$. We have for small ϵ and large x that

$$\begin{aligned} d_{EMD}(P, (1 - \epsilon)P + \epsilon\delta_x) &\approx \epsilon\|x\| \\ d_{2WD}(P, (1 - \epsilon)P + \epsilon\delta_x) &\approx \sqrt{\epsilon}\|x\| \\ d_{TV,\lambda}(P, (1 - \epsilon)P + \epsilon\delta_x) &\approx \epsilon \end{aligned}$$

Both EMD and smoothed TV have a linear dependence on ϵ while 2-Wasserstein has a square root dependence on ϵ . This means that 2-Wasserstein is much less robust to contamination for small ϵ . Meanwhile, only smoothed TV has an $O(1)$ dependence on $\|x\|$, meaning that smoothed TV is the most robust to outliers.

While the two properties of scale equivariance and robustness to outliers are only defined for Euclidean spaces, we will see that they are still useful for understanding the properties of the distance metrics in non-Euclidean settings, such as the projective plane.

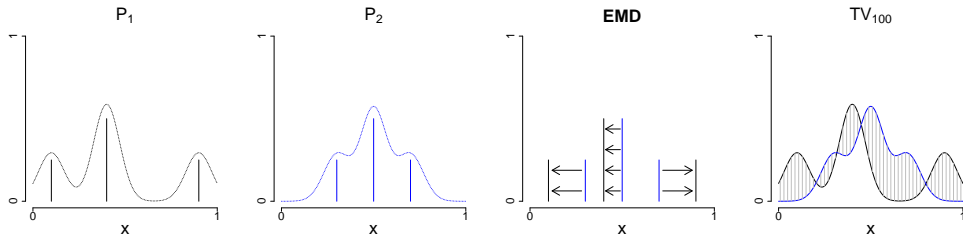


Figure 2: Schematic illustrating the difference between EMD and kernel-smoothed TV distance. Left to right: (i) probability distribution P_1 , a mixture of Dirac deltas (solid spikes), with kernel-smoothed form $P_{1,gauss,100}$ superimposed (dotted lines); (ii) distribution P_2 with smoothed form $P_{2,gauss,100}$ superimposed; (iii) computation of $d_{EMD}(P_1, P_2)$; (iv) computation of $d_{TV,gauss,100}(P_1, P_2) = d_{TV}(P_{1,gauss,100}, P_{2,gauss,100})$

2.3 Distances for fODFs

All of the aforementioned distance metrics can be adapted for the projective plane, and thus used to measure distances between fODFs.

Furthermore, both the EMD and 2WD equipped with the arc-length distance can be viewed as an extension of angular error (AE). If we take fODFs consisting of a single Dirac delta, both the angular error and the EMD distance between the fODFs is equal to the arc length distance between their directions: hence in figure 3, we see that EMD distance is linear with respect to AE; in contrast, RMSE, $TV_{gauss,1}$ and $TV_{gauss,100}$ are concave with respect to AE.

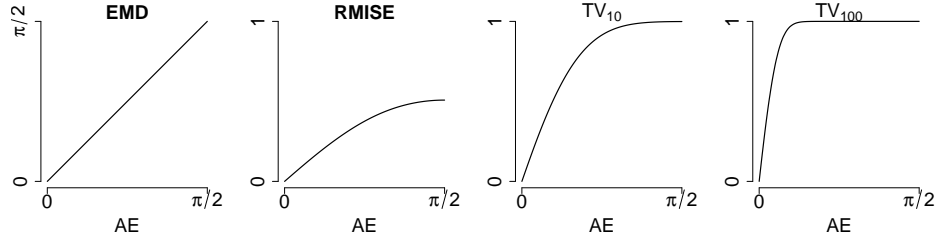


Figure 3: Distance between fODFs consisting of a single Dirac delta, $f_1 = \delta_v$, $f_2 = \delta_w$ as a function of $d_{arc}(v, w)$. Left to right: EMD, RMISE, $TV_{gauss,10}$, $TV_{gauss,100}$

2.4 Prediction error

Unlike other measures of accuracy, the prediction error of a model can be evaluated without knowing the ground truth, since it uses the observed data as a noisy version of the ground truth [12]. Furthermore, prediction error can be calculated using a single data set, via *cross-validation*.

Given data y_1, \dots, y_n corresponding to measurement directions x_1, \dots, x_n , one estimates the quantity \hat{S}_0 , e.g. by fitting the NLS model and setting $\hat{S}_0 = \|\beta\|_1$. The set of measurement directions x_1, \dots, x_n is partitioned into K disjoint sets A_1, \dots, A_K of roughly equal size, and resampled fODFs $\tilde{f}^1, \dots, \tilde{f}^K$, where \tilde{f}^i are obtained by estimating the fODF based only on the directions *not* in the set A_i . Each of the resampled fODFs \tilde{f}^j is used to make a prediction on the measurements in the *left-out set* $\{y_i : i \in A_j\}$. The cross-validated RMSE (CVRMSE) is computed as:

$$CVRMSE = \sum_{j=1}^K \sum_{i \in A_j} \left(y_i - \hat{S}_0 \int_v \exp(-\kappa(x'_i v)^2) d\tilde{f}^j(v) \right)$$

Alternatively, if two or more replicate measurements y^1, y^2 are available, one can also evaluate the replicated RMSE (RRMSE), defined by $RRMSE = \sum_{i=1}^n \left(y_i^2 - \hat{S}_0 \int_v \exp(-\kappa(x'_i v)^2) d\tilde{f}^1(v) \right)$. The CVRMSE and RRMSE differ only slightly in terms of mean; the RRMSE has smaller variance.

Supposing that the model is correctly specified, CVRMSE is an nearly unbiased estimate of the root mean integrated squared error (RMISE) from the noise-free signal. The RMISE is defined as the L_2 distance between smoothed measures: $d_{RMISE}(f_1, f_2) = \sqrt{\int_w (f_{1,ST,\kappa}(v) - f_{2,ST,\kappa}(v))^2 dv}$ where the smoothing kernel is computed from the Stejskal-Tanner equation [1] with a single shape parameter κ : $f_{ST,\kappa}(v) = \int_w \exp(-\kappa(v'w)^2) df(w)$.

2.5 Resampled Barycenters

If one had an accurate Bayesian model of the data, one could obtain an optimal estimate of the fODF with respect to expected EMD inaccuracy by obtaining the *Wasserstein barycenter* of the posterior distribution:

$$\hat{f} = \min_{\hat{f}} \int_f d_{EMD}(f, \hat{f}) dp(f|y) \quad (3)$$

, where $p(f|y)$ is the posterior distribution of the fODF with respect to the data y . The precise form of the posterior distribution appearing in (3) depends on the particular prior used. Bayesian approaches for DWI imaging [8] commonly use priors consisting of mixtures of K dirac deltas, where K also possibly has a prior distribution. The numerical computation of the Bayesian barycenter can be achieved by obtaining a large number of posterior samples f^1, \dots, f^N from the posterior, then solving

$$\hat{f} = \min_{\hat{f}} \frac{1}{N} \sum_{i=1}^N d_{EMD}(f^i, \hat{f}) dp(f|y) \quad (4)$$

A variety of approaches exist for solving the equation (4), including linear programming⁴, and a recent approach by Cuturi [14]. However, obtaining the posterior draws f^1, \dots, f^N may be extremely expensive.

One can bypass the computational cost of computing the posterior by exploiting the connection between Bayesian inference and resampling techniques. Efron [13] demonstrates a close connection between the parametric bootstrap and Bayesian posteriors for uninformative priors. The parametric bootstrap can be immediately applied to our setting: given an estimated fODF \hat{f}^0 , and an estimate of the noise $\hat{\sigma}^2$, generate synthetic bootstrap data y^1, \dots, y^K by $y_i^j \sim \text{Rician}\left(\int_v \exp(-\kappa(v'x_i)^2) d\hat{f}^0(v), \hat{\sigma}^2\right)$. Fitting the model to each synthetic bootstrap replicate y^1, \dots, y^K , obtain bootstrap estimates of the fODF $\hat{f}^1, \dots, \hat{f}^K$. Treating these bootstrap estimates as a sample from an approximate posterior, compute $\hat{f} = \min_f \sum_{i=1}^B d_{EMD}(f, \hat{f}^B)$. An alternate approach, and one which appears to be more effective in simulations, is to use K -fold partitioning rather than parametric bootstrap: that is, to obtain $\hat{f}^1, \dots, \hat{f}^K$ using the approach described in 2.4.

2.6 K-fold replicate error

The definition of replicate error requires at least two replicate measurements of the same voxel, $y^{(1)}$ and $y^{(2)}$: then given a distance function d , the replicate error is defined as $RE = d(\hat{f}^{(1)}, \hat{f}^{(2)})$. However, one can measure K-fold replicate error (K-RE) using a single set of measurements by using K-fold partitioning. Given a single set of measurements y , obtain $\hat{f}^1, \dots, \hat{f}^K$ according to the K -fold partitioning procedure described in 2.4. Then define the K -fold replicate error as follows:

$$\text{K-RE}_d = \frac{K-1}{\sqrt{K}} \left[\frac{1}{K(K-1)/2} \sum_{1 \leq i < j \leq K} d(\hat{f}^i, \hat{f}^j) \right]$$

The correction factor, $\frac{\sqrt{K}}{K-1}$, is used to reduce the dependence of the calculated replicate error on the arbitrary choice of K . Supposing the correction were not employed, the K -fold replicate error would be asymptotically proportional to $\sqrt{(K-1)}/K$, which is the product of the square root of the relative sample size $\sqrt{K/K-1}$ and the inverse proportion of directions shared between different folds, $1/(K-1)$.

3 Results and Discussion

3.1 Comparison of models and accuracy measures

We compare measures of accuracy applied to simulated estimates of fiber orientation distribution functions (fODF) obtained from different models. The measures we consider are angular error

⁴ In the case that fODFs $\hat{f}^1, \dots, \hat{f}^K$ are mixtures of Dirac deltas, it is possible to compute the Wasserstein barycenter using standard linear program solvers. Let v_i^j be the i th direction in the fODF \hat{f}^j , and w_i^j its corresponding weight, and let k_i denote the number of directions in \hat{f}^j . Let u_1, \dots, u_p be a dense sampling on the projective plane. Then the Wasserstein barycenter is found by the following optimization problem:

$$\begin{aligned} & \text{minimize} \sum_{\ell=1}^p \sum_{i=1}^K \sum_{j=1}^{k_i} x_{\ell ij} d_{arc}(u_\ell, v_i^j) \\ & \text{subject to} \sum_{\ell=1}^p x_{\ell ij} = w_i^j, w_\ell \geq 0, \sum_{i=1}^K \sum_{j=1}^{k_i} x_{\ell ij} = w_\ell \end{aligned}$$

for $\ell = 1, \dots, p$, $i = 1, \dots, K$ and $j = 1, \dots, k_i$. The output of the optimization problem is the values of the variables $x_{\ell ij}$ for $\ell = 1, \dots, p$, $i = 1, \dots, K$ and $j = 1, \dots, k_i$. The Wasserstein barycenter \hat{f}_{bar} can then be computed as follows.

1. Compute w_1, \dots, w_p , by $w_\ell \sum_{i=1}^K \sum_{j=1}^{k_i} x_{\ell ij}$
2. Let $\hat{f}_{bar} = \sum_{\ell=1}^p w_\ell \delta_{u_\ell}$

(AE), root mean integrated squared error (RMISE), earth mover’s distance (EMD), total variation (TV) with $\lambda = \{1, 10, 100\}$ and symmetric Kullback-Liebler (SKL) with $\lambda = \{1, 10, 100\}$ ⁵.

The ground truth fODF consists of two orthogonal directions with equal weights; the data was generated using parameters $\kappa = 1.5$ and $\sigma^2 = 0.04$. These parameters are typical for DWI simulations [2,4,5]. The simulated measurements used measurement directions x_1, \dots, x_{150} used in DWI measurements. We then fit a Bayesian model, best-2-subset and NNLS. The Bayesian prior was specified as described in 2.1, and the cross-validated barycenter was computed as described in 2.5 with $K = 20$ folds. Figure 1 displays sample model fits; Table 4 provides a table of the measures of accuracy of each model as averaged over 1000 random trials.

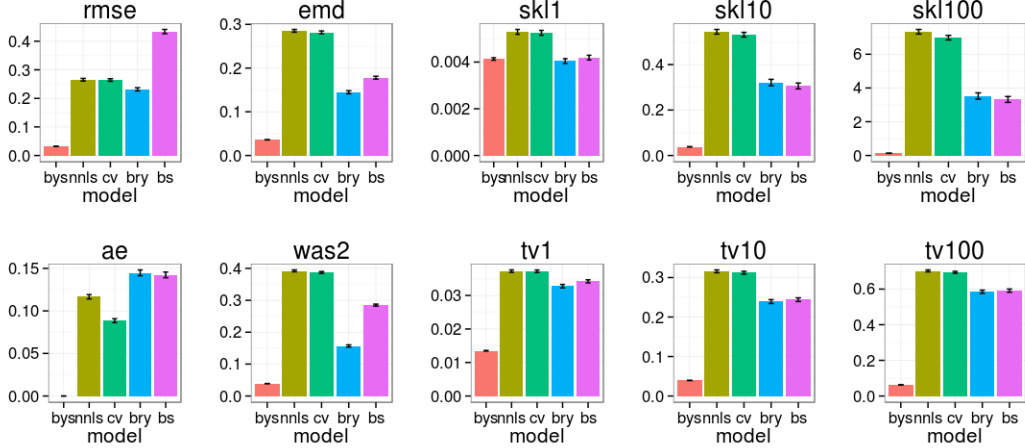


Figure 4: Simulated comparison of distance metrics. Models: Bayesian posterior mean (bys), Bayesian posterior Wasserstein barycenter (bry), best-2-subset (B2S), nonnegative least squares (NNLS), K-fold barycenter (cv). For comparison, see also Figure 1.

RMISE most strongly favors continuous estimates, such as the Bayes posterior mean. AE is undefined for continuous estimates and favors non-sparse estimates, such as NNLS and K-fold barycenter. On the opposite side of the spectrum, EMD favors sparse estimates, such as best-2-subset and the posterior barycenter. TV and SKL do not clearly favor sparse or non-sparse models. TV and SKL rank the models similarly regardless of the smoothing parameter used, but the smoothing parameter does influence the contrast between different methods. In the case of oversmoothing, all models have close to the minimum inaccuracy, as can be seen in the inaccuracies calculated using TV_1 and SKL_1 . In the case of undersmoothing, all models have close to the maximum inaccuracy, as seen in the inaccuracies calculated using TV_{100} and SKL_{100} . In the case of TV, we see that the ratio $\max \text{err} / \min \text{err}$ is equal to 1.3 for TV_1 , 1.3 for TV_{10} , and 1.2 for TV_{100} . In comparison, the ratio $\max \text{err} / \min \text{err}$ is equal to 1.9 for EMD.

The K-fold barycenter outperforms NNLS in all measures considered here: a somewhat surprising result, given that the K-fold barycenter was solely motivated by the goal of minimizing the inaccuracy as measured by EMD.

3.2 Correlation of error with replicate error

In a similar simulated experiment with $k = 2$ fiber directions, uniform random weight w_1 and $w_2 = 1 - w_1$, $\sigma^2 = 0.04$ and varying κ , we compare the correlations between errors $\text{err} = d(f, \hat{f}^1)$ and replicate errors $RE = d(\hat{f}^1, \hat{f}^2)$. We find that the correlation between the EMD-based error and EMD-based replicate error, $\text{Corr}(\text{err}_{EMD}, RE_{EMD})$ is above 0.4 for a range of parameter values κ from 0.1 to 2—higher than the minimum correlations for other distances. Figure 5 contains correlations, as computed from 10000 simulations, for several values of κ .

⁵ The choice of smoothing parameters λ for TV and SKL are somewhat arbitrary; we are not aware of any previous use of smoothed distances in the DWI literature.

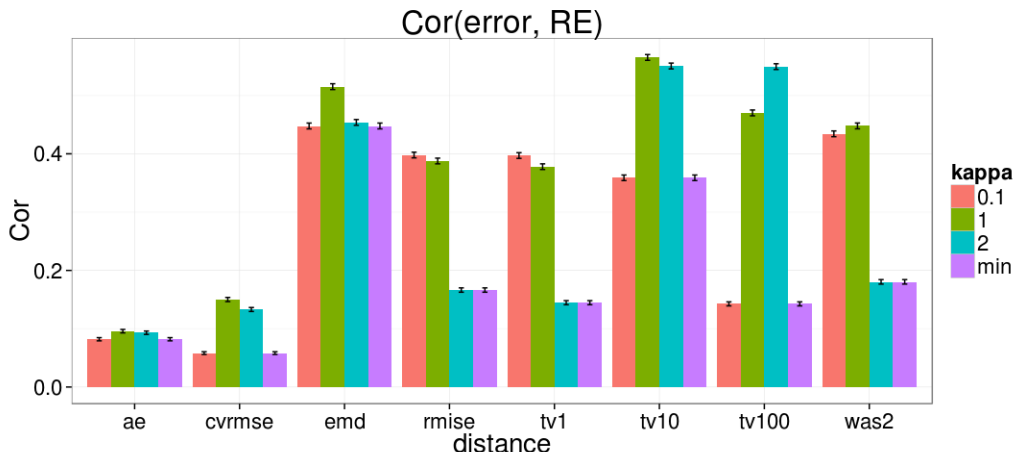


Figure 5: Correlation of error and replicate error for data generated from a simulation of a two-direction fODF. For each metric, the values at different κ are presented, and 'min' denotes the minimal correlation among the different values of κ for that metric. The column for RRMSE contains values for $\text{Corr}(RRMSE, RE_{RMISE})$. All other columns contain the correlation between err (error) and RE (replicate error) when both quantities are evaluated using the given distance/divergence.

Given the practical utility of RRMSE, it is surprising to see its low correlation with the true RMISE regardless of κ . Although RRMSE is a close-to-unbiased estimated of the err_{RMISE} , this may come at a cost of greater variability. In contrast, RE_{RMISE} has a much higher correlation with err_{RMISE} . At first glance RE_{RMISE} appears to be a very similar procedure to RRMSE, but while RRMSE compares the signal from replicate 1 with the raw data of replicate 2, RE_{RMISE} compares the signal from replicate 1 with the signal from replicate 2. The distance measure with the highest correlation between err and RE varies depending on κ . For $\kappa = 0.1$, EMD has the highest correlation, 0.45 ± 0.01 ; for $\kappa = 1$, TV_1 has the highest correlation: 0.55 ± 0.01 , slightly higher than EMD (0.52 ± 0.01), while for $\kappa = 2$, TV_{10} has the highest correlation: 0.55 ± 0.01 . In both TV and SKL we see that the choice of smoothing parameter which maximizes the correlation depends on κ . Meanwhile, the 2-Wasserstein distance, which does not use smoothing, nevertheless has poor correlation between err and RE at $\kappa = 2$, and is consistently dominated by EMD.

To summarize, the correlation of $\text{Corr}(\text{err}_{EMD}, RE_{EMD})$ is consistently comparable to the highest correlation of any other distance. Distances with fixed smoothing kernels suffer from degraded correlation at one of the extremes of the parameter range, $\kappa = 0.1$ or $\kappa = 2$, while the 2-Wasserstein distance also suffers from degraded correlation at high κ even though it does not employ smoothing; in contrast, EMD is robust across κ .

These results can seemingly be explained by the fact that EMD has a combination of *scale equivariance* and *robustness to outliers* as defined in section 2.2. Even though the two properties were only defined in the Euclidean setting, they can be extended in a 'local' sense to any manifold via the fact that manifolds resemble Euclidean space in a small neighborhood of any point. In the particular application of DWI fiber deconvolution, the consequence of scale equivariance is that the increased error due to increased noise level will be reflected both in the error and the replicate error. Interestingly, though, we found correlations between error and replicate error in the simulation even when holding the noise level fixed. This can be explained by the fact that even if the noise level is held fixed, changes in the parameter κ or the fiber configuration can mimic the effect of increased noise. Thus, the fact that smoothed TV and smoothed SKL are *not* scale equivariant explains their inconsistent performance across κ . Meanwhile, the poor performance of 2-Wasserstein distance for $\kappa = 2$ can be explained by the poor robustness of 2-Wasserstein distance to outliers. When κ is low, relative to the sample size (number of measurement directions), the NNLS algorithm finds very few 'spurious' directions. However, when κ is high relative to sample size, a noise spike in a single measurement direction can cause NNLS to weight an essentially arbitrary direction in a direction orthogonal to the direction of the noise spike. This leads to the production of 'outliers' for high

κ , which inflate the variance of the relative error as measured by 2-Wasserstein distance. On the other hand, these directional ‘artifacts’ can be removed by means of post-processing; hence it would still be interesting to revisit the application of the 2-Wasserstein distance on post-processed NNLS estimates.

3.3 Application to DWI data measured *in vivo*

DWI data was acquired in a healthy human participant in a 3T MRI instrument, at the Stanford Center for Neurobiological and Cognitive Imaging. Data was acquired at $2 \times 2 \times 2 \text{ mm}^3$ with a b-value of 2000 s/mm^2 . The data consists of two sets of replicate measurements⁶. We identified regions of interest for analysis in the corpus callosum (CC), a region of the brain known to contain only one major fascicle, connecting the two cerebral hemispheres, and in the centrum semiovale (CSO), a part of the brain in which multiple fascicles cross. We compute K-fold replicate error ($K = 10$), and replicate error of the fODF estimates. We also compute CVRMSE as a direct estimate of accuracy (with regard to RMISE). A value of $\kappa = 2.2$ was estimated using cross-validation on a separate subset of the data.

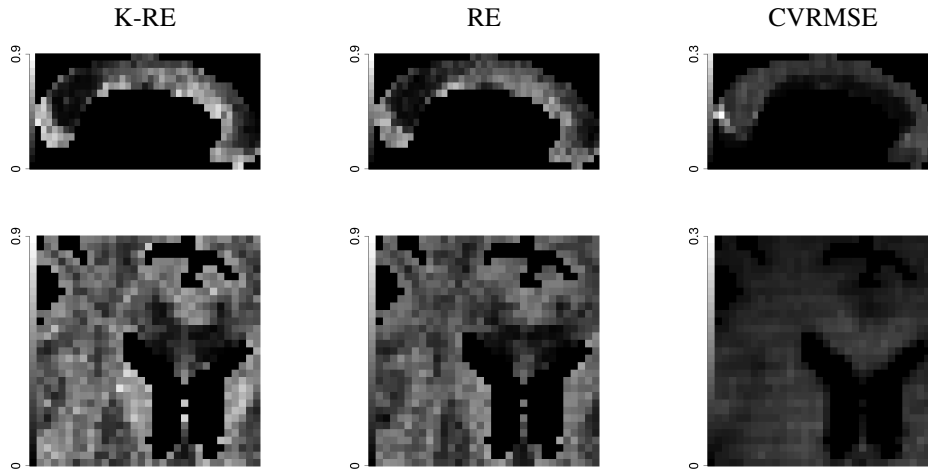


Figure 6: Empirical measures of replicate error (EMD) and prediction error (CVRMSE) by brain region. Top row: Sagittal view of the corpus callosum (CC), a part of the brain that contains fibers connecting the two cerebral hemispheres. Bottom row: Axial view of the centrum semiovale (CSO), a part of the brain that contains multiple crossing fiber populations

CVRMSE appears to vary more smoothly across both regions of interest in the white matter. On the other hand, measures of replicate error (both RE and K-RE) show more coherent spatial variation. Both CVRMSE and replicate error are sensitive both to the configuration of the fibers in the measurement voxel and to the noise in the measurement, but their sensitivities to these factors differ. While CVRMSE is primarily sensitive to noise, EMD-based replicate error is more sensitive to the configuration of the underlying tissue (i.e. single fiber population, or more populations of fibers). The spatial variations in EMD across the corpus callosum ROI represent, therefore, variations in the degree to which different parts of the measurement contain partial volumes of other neighboring parts of the tissue. These other parts may contain either cerebrospinal fluid (the fluid the surrounds and pervades the brain), or fibers oriented in other directions than the corpus callosum fibers. The measurement noise, on the other hand, is dominated by physiological factors, and instrumental factors that vary very little across space. Hence, the relative smoothness of the variation of CVRMSE across these regions.

⁶The data is available to download at: <http://purl.stanford.edu/ng782rw8378>

4 Conclusions

In this paper we address the question of selecting an error metric for fODF estimation. Through simulations, we illustrate the differences between EMD and alternative metrics, such as smoothed total variation and RMISE. EMD favors sparse estimates of the fODF, and is an intuitive extension of angular error, which is commonly used to characterize accuracy in the DWI literature. These properties favor the use of EMD in theoretical work and simulations. In practice, one might only be able to measure replicate error, or K-fold replicate error. Use of the EMD in practical applications, on empirical data, is supported by the consistent correlation of approximately 0.4 between replicate error and error as measured by EMD across a wide range of experimental conditions and biological factors (embodied in the model parameterization by κ). Other error metrics, such as smoothed total variation distance, may have higher correlation between replicate error and error, but this depends on the smoothing parameter λ . EMD has a unique combination of scale equivariance and robustness to outliers, which further supports the use of EMD-based replicate error as a proxy for EMD-based error. The use of EMD as an error metric motivates the use of Wasserstein barycenters as estimates of the fODF: while the K-fold barycenter is motivated as an approximation to the Bayesian posterior barycenter, we find in simulations that the K-fold barycenter outperforms NNLS in all measures of accuracy considered, hence meriting more detailed investigation of its properties.

Acknowledgments

The authors thank Trevor Hastie, Brian Wandell, Eero Simoncelli, Justin Solomon, Leo Guibas and Shuo Xie for useful discussions, and the anonymous referees for their helpful suggestions. CZ was supported through an NIH grant 1T32GM096982 to Robert Tibshirani and Chiara Sabatti, AR was supported through NIH fellowship F32-EY022294. FP was supported through NSF grant BCS1228397 to Brian Wandell

References

- [1] Le Bihan D, Mangin JF, Poupon C, Clark CA, Pappata S, Molko N, Chabriat H. (2001). Diffusion tensor imaging: concepts and applications. *Journal of magnetic resonance imaging*, 13(4), 534-546.
- [2] Tournier J-D, Calamante F, Connelly A (2007). Robust determination of the fibre orientation distribution in diffusion MRI: non-negativity constrained super-resolved spherical deconvolution. *Neuroimage* 35:145972
- [3] Tournier, J.-D., Yeh, C.-H., Calamante, F., Cho, K.-H., Connelly, A., and Lin, C.-P. (2008). Resolving crossing fibres using constrained spherical deconvolution: validation using diffusion-weighted imaging phantom data. *NeuroImage*, 42: 61725.
- [4] Basser PJ. Quantifying errors in fiber-tract direction and diffusion tensor field maps resulting from MR noise. *Proc. Int. Soc. Magn. Reson. Med.* 1997
- [5] Aganj I, Lenglet C, Jahanshad N, Yacoub E, Harel N, Thompson PM, Sapiro G. (2011). A Hough transform global probabilistic approach to multiple-subject diffusion MRI tractography. *Medical image analysis*, 15(4), 414-425.
- [6] Frank L. Anisotropy in high angular resolution diffusion-weighted MRI. *Magnetic Resonance in Medicine* Volume 45, Issue 6, pages 935939, June 2001
- [7] DellAcqua F, Rizzo G, Scifo P, Clarke RA, Scotti G, Fazio F (2007). A model-based deconvolution approach to solve fiber crossing in diffusion-weighted MR imaging. *IEEE Trans Biomed Eng* 54:46272
- [8] Behrens TEJ, Berg HJ, Jbabdi S, Rushworth MFS, and Woolrich MW (2007). Probabilistic diffusion tractography with multiple fiber orientations: What can we gain? *NeuroImage* (34):144-45.
- [9] Gudbjartsson, H., and Patz, S. (1995). The Rician distribution of noisy MR data. *Magn Reson Med.* 34: 910914.
- [10] Parzen E. On the estimation of a probability density function and mode. *The Annals of Mathematical Statistics.* 33(3): 1065-1076, 1962.

- [11] Rubner, Y., Tomasi, C. Guibas, L.J. (2000). The earth mover's distance as a metric for image retrieval. *Intl J. Computer Vision*, 40(2), 99-121.
- [12] Rokem A, Yeatman J, Pestilli F, Kay K, Mezer A, van der Welt S, Wandell B. (2013). Evaluating the accuracy of models of diffusion MRI in white matter. Submitted.
- [13] Efron B. Bayesian inference and the parametric bootstrap. *The Annals of Applied Statistics* 6 (2012), no. 4, 1971–1997.
- [14] Cuturi M, Doucet A. Fast computation of Wasserstein barycenters. *JMLR W&CP* 32 (1) : 685693, 2014